

# Penetration and lateral diffusion characteristics of polycrystalline graphene barriers†

Cite this: *Nanoscale*, 2014, 6, 151Taeshik Yoon,<sup>a</sup> Jeong Hun Mun,<sup>b</sup> Byung Jin Cho<sup>\*bc</sup> and Taek-Soo Kim<sup>\*ac</sup>

Received 25th July 2013

Accepted 20th October 2013

DOI: 10.1039/c3nr03849a

[www.rsc.org/nanoscale](http://www.rsc.org/nanoscale)

We report penetration and lateral diffusion behavior of environmental molecules on synthesized polycrystalline graphene. Penetration occurs through graphene grain boundaries resulting in local oxidation. However, when the penetrated molecules diffuse laterally, the oxidation region will expand. Therefore, we measured the lateral diffusion rate along the graphene–copper interface for the first time by the environment-assisted crack growth test. It is clearly shown that the lateral diffusion is suppressed due to the high van der Waals interaction. Finally, we employed bilayer graphene for a perfect diffusion barrier facilitated by decreased defect density and increased lateral diffusion path.

Graphene has been regarded as a superior diffusion barrier<sup>1–5</sup> due to its atomic structure, which is composed of densely packed carbon atoms.<sup>6–8</sup> Synthesized graphene<sup>2,3</sup> and rGO (reduced graphene oxide) multilayers<sup>1,4,9</sup> have been adopted as gas diffusion barriers, which showed extremely high resistance to molecular penetration. As barrier layers, graphene provides additional advantages in real applications. One-atom-thickness overcomes dimension constraints from an engineering perspective, and transparency enables optical applications. Furthermore, extremely low bending stiffness ensures conformal contact with arbitrary surfaces. Large-area graphene<sup>10–13</sup> synthesized for the purpose of a diffusion barrier is basically polycrystalline, and therefore has numerous graphene grain boundaries (GGBs).<sup>14–19</sup> However, these GGBs are potentially vulnerable to the penetration of molecules because their chemical structures are modified, with larger vacancies or non-carbon atoms.<sup>19,20</sup> It has been reported that the modified GGB structure significantly reduces the activation energy of

diffusion,<sup>19</sup> and as a result, metal oxidation occurs since environmental molecules such as oxygen or water will tend to penetrate into the graphene membrane. GGBs are critical defects, which should be considered before using graphene as a diffusion barrier. Furthermore, lateral diffusion of the penetrating molecules along the interface between graphene and metal is also a critical concern. Once lateral diffusion occurs, oxidation along the interface will be accelerated, which will further lead to delamination of the graphene barrier from the metal.<sup>21,22</sup> Although it is known that a graphene surface enables the ultrafast diffusion of water molecules even at low temperature,<sup>23,24</sup> a recent study showed that water molecules can be stably trapped at the interface between graphene and mica, which implies that lateral diffusion is unfavorable.<sup>25</sup> To the best of our knowledge, an investigation of the lateral diffusion of penetrating environmental molecules between as-grown graphene and copper, which is critical for the passivation, has not been reported.

Here, we show the penetration of molecules on GGBs and their lateral diffusion along the graphene–metal interface. To visualize GGBs on the metal, as-grown graphene on the metal was heated, and the temperature dependent oxidation of the metal on GGBs was observed. Monolayer and bilayer graphene were utilized for metal passivation, and the bilayer graphene on the metal showed superior resistance to oxidation when compared with that of monolayer graphene. The lateral diffusion of molecules between graphene and metal was measured by the environment-assisted crack growth test.<sup>26–29</sup> Through these analyses, the barrier mechanism of graphene is explained, and we discuss why graphene is still a superior diffusion barrier even though it has numerous GGBs.

To visualize GGBs, as-grown graphene on the metal was heated to induce metal oxidation. The test procedure is shown in Fig. 1. A 300 nm thick copper film was deposited on a silicon wafer, and then graphene was synthesized by the chemical vapor deposition (CVD) method.<sup>29</sup> The scanning electron microscope (SEM) image in Fig. 1a shows the as-grown graphene on copper, and the copper has grains of a

<sup>a</sup>Department of Mechanical Engineering, KAIST, Daejeon 305-701, Korea. E-mail: [tskim1@kaist.ac.kr](mailto:tskim1@kaist.ac.kr)

<sup>b</sup>Department of Electrical Engineering, KAIST, Daejeon 305-701, Korea. E-mail: [bjcho@ee.kaist.ac.kr](mailto:bjcho@ee.kaist.ac.kr)

<sup>c</sup>Graphene Research Center (GRC), KAIST, Daejeon 305-701, Korea

† Electronic supplementary information (ESI) available. See DOI: 10.1039/c3nr03849a

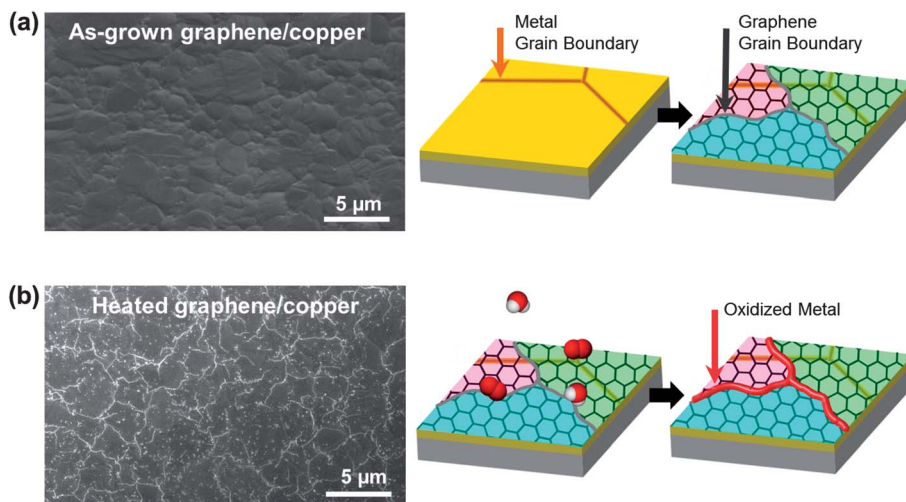


**Fig. 1** Visualizing graphene grain boundaries by heating graphene on a metal. (a) SEM image of the as-grown graphene on copper. (b) SEM image of the heated graphene on copper. The bright lines are metal oxide formed on GGBs by penetration of environmental molecules.

few-micron-size. As shown in Fig. 1b, the graphene on the metal was then heated in controlled lab air containing oxygen and water molecules. We observed that no meaningful changes appeared in the SEM images until heating reached 100 °C. However, when the temperature was over 150 °C, bright lines formed on the surface of the graphene, as shown in the SEM image of Fig. 1b. The bright lines are metal oxide which grew at the GGBs following the penetration of molecules. This result clearly shows that molecules can easily penetrate into the GGBs, and react with the metal at high temperature. Therefore, even though graphene is a superior oxidation barrier, GGBs are vulnerable to molecular diffusion.

The key issue in visualizing GGBs is determining whether the formed lines are GGBs or metal grain boundaries. We used atomic force microscopy (AFM) for morphology mapping of the heated multilayer. Representative AFM images of the heated graphene–copper surface are shown in Fig. 2. Fig. 2a and b show low-magnification topography and high-magnification phase images, respectively. The metal grain boundaries can be observed as the dark and concave lines in Fig. 2a and c, while metal oxide lines are bright and convex. The lines formed on GGBs are connected with other lines, and Fig. 2c shows the junction of triple GGBs. The junction exists on a single grain of the metal, and the line profiles of Fig. 2c are shown in Fig. 2d. From these results, it can be clearly seen that the formed metal lines do not coincide with the metal grain boundaries. Therefore, the oxidized lines formed on GGBs are independent of the location and shape of metal grain boundaries. These results agree with recent research about the relationship of GGBs and metal grain boundaries.<sup>19</sup>

To observe the effect of temperature on metal passivation, our heating temperature was varied from 150 °C to 200 °C. Fig. 3a–c show that the metal oxide lines on GGBs get thicker as the heating temperature increases. Fig. 3d and e show the width and height of the formed lines, which were measured by AFM profiling. As in the SEM images, the line width and height are strongly dependent on the heating temperature. High

temperature enhanced penetration of environmental molecules through GGBs can be well explained by a thermally activated diffusion process.

Synthesized large-area graphene has numerous GGBs on the plane, and these become line defects during metal passivation. To obtain higher passivation performance with graphene, we propose a method of stacking bilayer graphene on the metal to

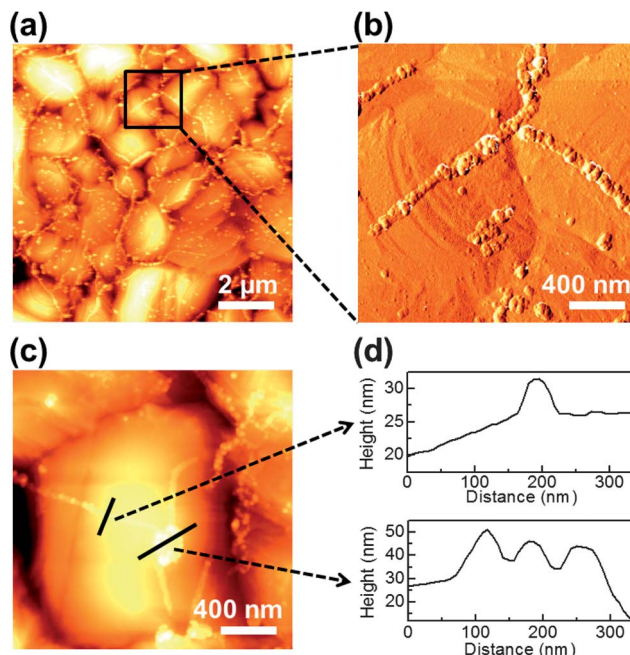


**Fig. 2** Morphology mapping of the metal oxide lines on graphene grain boundaries by AFM. (a) Low-magnification topography image showing the visualized GGBs on the metal. (b) High-magnification phase image showing that the location of GGBs is independent of the metal grain boundaries. (c) High-magnification topography image showing that triple GGBs are connected on a single metal grain. (d) Height profiles of the formed metal oxide lines marked in (c).

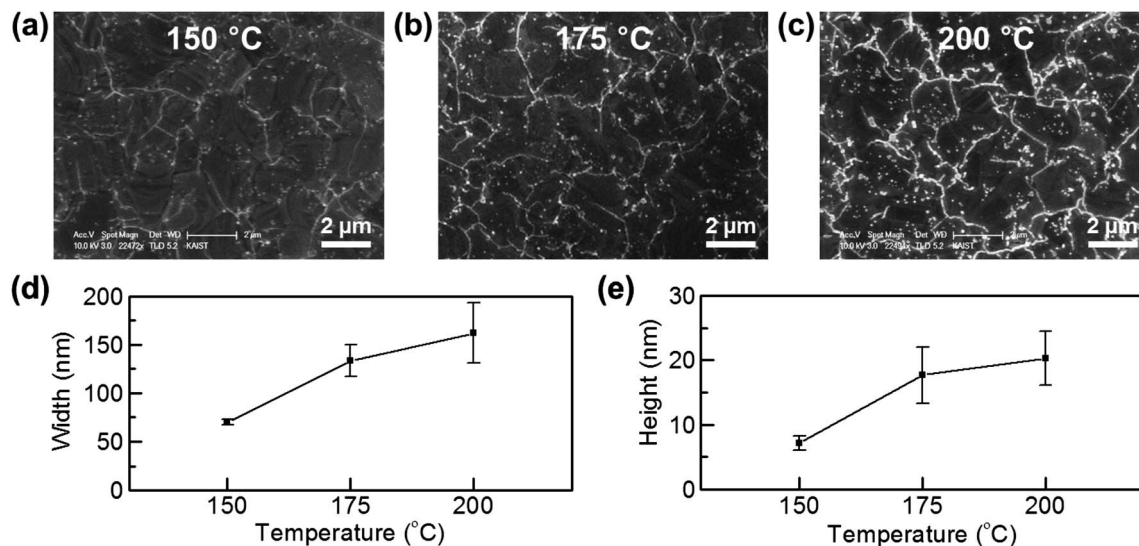


Fig. 3 Evolution of the metal oxide lines with temperature. SEM images of the heated graphene on copper (a–c). The heating temperatures are 150 °C (a), 175 °C (b) and 200 °C (c). The dimensions of the lines are measured by AFM (d and e). The width (d) and height (e) of the oxidized metal lines are plotted.

minimize these defects. While graphene is composed of line defects, when another graphene layer is added to the surface, only point defects can occur at the intersection of line defects from two separate graphene layers. Therefore, this method effectively reduces penetration of the environmental molecules. Furthermore, a longer diffusion path is required for environmental molecules to reach the metal; hence oxidation can be retarded.

Bare copper, monolayer graphene on copper, and bilayer graphene on copper were prepared to evaluate metal passivation. The bilayer sample was prepared by transferring monolayer graphene onto an already grown monolayer graphene–metal specimen.<sup>11,13</sup> The number of graphene layers was reconfirmed by Raman spectra.<sup>30</sup> As shown in Fig. 4d, the peak intensities of G and 2D are almost the same in the bilayer graphene, while the 2D peak is stronger than the G peak in the monolayer graphene. Same heating conditions of 200 °C and 3 minutes were used for each sample. Fig. 4a shows the bare metal without graphene: the entire metal surface is covered by metal oxide and the metal's original morphology has disappeared. In the case of monolayer graphene on copper, it can effectively block oxidation except for the GGB region, as shown in Fig. 4b. However, the results of the bilayer graphene sample in Fig. 4c do not show any oxidized area. This means that the metal is perfectly protected by the bilayer graphene by increased lateral diffusion path and reduced defect sites. This result is notably promising because the deleterious effects of GGBs in polycrystalline graphene can be simply eliminated by just adding a graphene layer, which does not impede the advantages of using graphene.

So far, the penetration of molecules into the graphene membrane has been addressed; however, lateral diffusion along the graphene–metal interface should also be considered for a better understanding of the passivation mechanism. We found that the environmental molecules can easily penetrate into the

graphene membrane *via* GGBs, even though graphene has superior impermeability. Furthermore, if the penetrated molecules are mobile on the graphene–metal interface, oxidation will be accelerated and the passivation will be eventually useless. For this reason, lateral diffusion should be quantitatively measured and studied. However, it has not been previously reported because of the difficulty of accurately controlling the interface.

In our study, the graphene–metal interface was mechanically opened for measurement of the lateral diffusion rate by an environment-assisted crack growth test. The lateral diffusion of molecules gives rise to interface debonding, and finally a crack is propagated. The lateral diffusion rate is equivalent to the crack growth rate, which can be measured by the environment-assisted crack growth test.<sup>26–28</sup> The specimen structure<sup>29</sup> is shown in the inset of Fig. 5a, and further information is provided in the environment-assisted crack growth test discussion in the Experimental section. The test conditions were RH (Relative Humidity) values of 50%, 70% and 90% with a fixed temperature of 30 °C.

The crack growth rate was measured with the applied strain energy release rate as shown in Fig. 5a. The applied strain energy release rate ( $G$ ) is the factor of loading condition at the crack tip, which is related to crack length, dimensions, and applied load. The threshold  $G$  is determined when the crack starts to propagate, which was found to be  $0.7 \text{ J m}^{-2}$ . This value exactly corresponds to the adhesion energy of graphene–copper,<sup>29</sup> which indicates that the crack growth was not affected by environmental molecules;<sup>27</sup> therefore there was no meaningful difference for the three RH conditions. The measured minimum crack growth rate was  $10^{-11} \text{ m s}^{-1}$ , which is the lower limit of our measurement system. This means that the lateral diffusion rate will be lower than  $10^{-11} \text{ m s}^{-1}$  when the  $G$  is lower than the energy of graphene–copper. In other words, the environmental molecules hardly diffuse unless the interface is

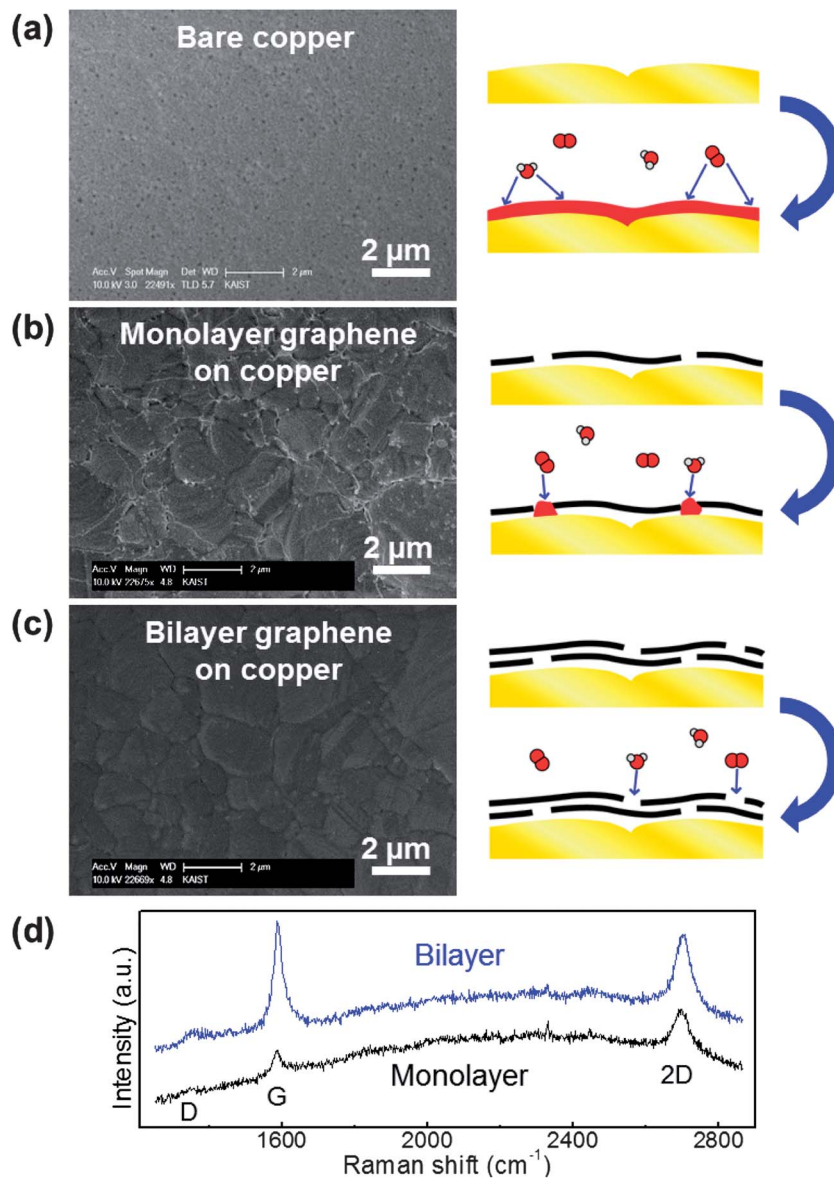


Fig. 4 Stacking graphene layers for metal passivation. SEM images after heating (a–c). The specimen structures are bare copper (a), monolayer graphene on copper (b) and bilayer graphene on copper (c). The bilayer graphene can effectively block the environmental molecules, while oxidized metal lines are formed on GGBs in the monolayer graphene specimen. (d) Raman spectra of monolayer and bilayer graphene on copper.

mechanically opened, and do not affect the adhesion energy of graphene–copper. To the best of our knowledge, this is the first reported measurement of lateral diffusion between as-grown graphene on copper, and it reveals the lateral diffusion suppressing ability of graphene. It has been reported that lateral diffusion along the graphene oxide layers yields a rate on the order of  $10^{-4} \text{ m s}^{-1}$  (ref. 31), which is seven orders of magnitude higher than our result,  $10^{-11} \text{ m s}^{-1}$ . This comparison clearly suggests that the as-grown graphene on the metal is truly an ideal barrier to lateral diffusion. The suppression of lateral diffusion can also be confirmed by the previous study which found that water molecules become immobile between pristine graphene and mica.<sup>25</sup>

The atomic-scale schematic of the crack tip is shown in Fig. 5b. Although environmental molecules can freely diffuse

into a mechanically opened region, they hardly diffuse into a pristine interface region. The graphene effectively impedes the lateral diffusion of molecules because the high van der Waals interaction between graphene and metal<sup>29,32</sup> results in a high activation energy for the lateral diffusion of molecules. According to the previous results discussed in this paper, the suppressed lateral diffusion plays an important role in metal passivation. Experimental results clearly show that the suppressed lateral diffusion prevents further spreading of the oxidation region, although the penetration of molecules occurs on GGBs in monolayer graphene. Furthermore, bilayer graphene can eliminate this penetration by increasing lateral diffusion path and reducing defect sites.

In conclusion, we have characterized the penetration and lateral diffusion of polycrystalline graphene used as a diffusion

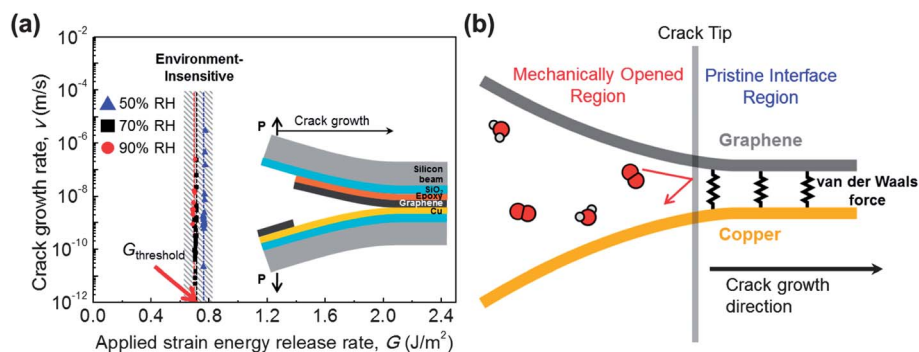


Fig. 5 Lateral diffusion of environmental molecules along the graphene–copper interface. (a) Environment-assisted crack growth test of the graphene–copper interface. The crack growth rate is measured as a function of the applied strain energy release rate. The specimen structure is shown in the inset. The threshold  $G$  is equal to the adhesion energy of the interface, which means that the lateral diffusion hardly occurs unless the interface is mechanically opened. (b) Atomic-scale schematic of the crack tip. The molecules can freely diffuse through the mechanically opened region while the van der Waals force of graphene suppresses lateral diffusion along the pristine interface.

barrier. Graphene defects were visualized by the penetration of molecules on GGBs, a method which can be used directly for evaluating synthesized graphene. Even though the GGBs enabled metal oxidation, it was arrested by stacking bilayer graphene. The measured lateral diffusion rate along the as-grown graphene–copper interface was lower than that of the graphene oxide interface by seven orders of magnitude, which reveals that polycrystalline graphene is still an ideal diffusion barrier.

## Experimental section

### Graphene synthesis and sample preparation

Graphene layers were synthesized by the CVD method.<sup>10,11,33</sup> For the catalytic substrate, a Cu (300 nm) thin film was deposited sequentially on an oxidized silicon wafer. After the *in situ* cleaning process of H<sub>2</sub> plasma annealing, the sample was annealed at 700 °C for 2 min. The pressure was maintained at 50 mTorr, and the precursor gases were Ar : C<sub>2</sub>H<sub>2</sub> = 40 : 1. For the preparation of bilayer graphene on a Cu thin film, one graphene layer was transferred onto another graphene grown Cu sample by a wet transfer method.<sup>33,34</sup>

### Environment-assisted crack growth test

The specimen structure is based on the double cantilever beam (DCB) test, which enables symmetric beam bending. A graphene–Cu–silicon wafer was prepared, and a same size dummy silicon wafer was also prepared. The epoxy adhesive (Epo-Tek 353nd) was used for bonding both wafer beams, and was cured in a convection oven. Aluminum loading tabs were attached on each side of beams for coupling the specimen with the micro-mechanical test system (Delaminator Adhesion Test System; DTS Company), which is composed of linear actuator and load-cell. The whole system was then put into an environmental chamber with controlled temperature and humidity. The crack can be propagated by tensile motion of the linear actuator. After initial crack propagation, the load relaxation was measured while the displacement was fixed. The load decreased with crack propagation; the crack growth rate can be measured as a function of the applied strain energy release rate as shown in Fig. 5a.

### Surface characterization methods

For the characterization of graphene on the metal, we utilized Raman spectroscopy. The ARAMIS (Horiba Jobin Yvon, France) equipment was used, and an Ar ion laser beam (514.5 nm) was irradiated on graphene–Cu surfaces. The obtained spectrum ranged from 1000 cm<sup>-1</sup> to 3000 cm<sup>-1</sup>, and each spectrum was acquired twenty times. A field-emission scanning electron microscope (FE-SEM) was used for visualizing metal oxidation. The 10 kV electron beam with 22 500× magnification was used to observe oxidized metal lines of sub-micron thickness. Finally, the morphology of visualized metal oxide lines was characterized using atomic force microscopy (XE-100, Park Systems, Korea). The topography and phase images were obtained using non-contact mode, and the 100 μm<sup>2</sup> area was scanned on each sample.

## Acknowledgements

This work was supported by National Research Foundation of Korea (NRF) Research Grants 2012-R1A1A1006072, 2013-H1A2A1032731, 2010-0029132, and 2011-0031638.

## References

- 1 H. Kim, Y. Miura and C. W. Macosko, *Chem. Mater.*, 2010, **22**, 3441–3450.
- 2 E. Sutter, P. Albrecht, F. E. Camino and P. Sutter, *Carbon*, 2010, **48**, 4414–4420.
- 3 S. Chen, L. Brown, M. Levendorf, W. Cai, S.-Y. Ju, J. Edgeworth, X. Li, C. W. Magnuson, A. Velamakanni and R. D. Piner, *ACS Nano*, 2011, **5**, 1321–1327.
- 4 L. Qiu, X. Zhang, W. Yang, Y. Wang, G. P. Simon and D. Li, *Chem. Commun.*, 2011, **47**, 5810–5812.
- 5 F. Guo, G. Silverberg, S. Bowers, S.-P. Kim, D. Datta, V. Shenoy and R. H. Hurt, *Environ. Sci. Technol.*, 2012, **46**, 7717–7724.
- 6 K. Novoselov, A. K. Geim, S. Morozov, D. Jiang, Y. Zhang, S. Dubonos, I. Grigorieva and A. Firsov, *Science*, 2004, **306**, 666–669.

- 7 A. K. Geim and K. S. Novoselov, *Nat. Mater.*, 2007, **6**, 183–191.
- 8 J. S. Bunch, S. S. Verbridge, J. S. Alden, A. M. van der Zande, J. M. Parpia, H. G. Craighead and P. L. McEuen, *Nano Lett.*, 2008, **8**, 2458–2462.
- 9 H. M. Kim, J. K. Lee and H. S. Lee, *Thin Solid Films*, 2011, **519**, 7766–7771.
- 10 A. Reina, X. Jia, J. Ho, D. Nezich, H. Son, V. Bulovic, M. S. Dresselhaus and J. Kong, *Nano Lett.*, 2008, **9**, 30–35.
- 11 K. S. Kim, Y. Zhao, H. Jang, S. Y. Lee, J. M. Kim, K. S. Kim, J.-H. Ahn, P. Kim, J.-Y. Choi and B. H. Hong, *Nature*, 2009, **457**, 706–710.
- 12 X. Li, W. Cai, J. An, S. Kim, J. Nah, D. Yang, R. Piner, A. Velamakanni, I. Jung and E. Tutuc, *Science*, 2009, **324**, 1312–1314.
- 13 S. Bae, H. Kim, Y. Lee, X. Xu, J.-S. Park, Y. Zheng, J. Balakrishnan, T. Lei, H. R. Kim and Y. I. Song, *Nat. Nanotechnol.*, 2010, **5**, 574–578.
- 14 R. Grantab, V. B. Shenoy and R. S. Ruoff, *Science*, 2010, **330**, 946–948.
- 15 O. V. Yazyev and S. G. Louie, *Nat. Mater.*, 2010, **9**, 806–809.
- 16 P. Y. Huang, C. S. Ruiz-Vargas, A. M. van der Zande, W. S. Whitney, M. P. Levendorf, J. W. Kevek, S. Garg, J. S. Alden, C. J. Hustedt and Y. Zhu, *Nature*, 2011, **469**, 389–392.
- 17 D. W. Kim, Y. H. Kim, H. S. Jeong and H.-T. Jung, *Nat. Nanotechnol.*, 2011, **7**, 29–34.
- 18 K. Kim, Z. Lee, W. Regan, C. Kisielowski, M. Crommie and A. Zettl, *ACS Nano*, 2011, **5**, 2142–2146.
- 19 D. L. Duong, G. H. Han, S. M. Lee, F. Gunes, E. S. Kim, S. T. Kim, H. Kim, Q. H. Ta, K. P. So and S. J. Yoon, *Nature*, 2012, **490**, 235–239.
- 20 M. E. Suk and N. Aluru, *J. Phys. Chem. Lett.*, 2010, **1**, 1590–1594.
- 21 P. A. Sørensen, K. Dam-Johansen, C. Weinell and S. Kiil, *Prog. Org. Coat.*, 2010, **67**, 107–115.
- 22 P. Sutter, J. T. Sadowski and E. A. Sutter, *J. Am. Chem. Soc.*, 2010, **132**, 8175–8179.
- 23 J. Ma, A. Michaelides, D. Alfe, L. Schimka, G. Kresse and E. Wang, *Phys. Rev. B: Condens. Matter Mater. Phys.*, 2011, **84**, 033402.
- 24 J. H. Park and N. Aluru, *J. Phys. Chem. C*, 2010, **114**, 2595–2599.
- 25 K. Xu, P. Cao and J. R. Heath, *Science*, 2010, **329**, 1188–1191.
- 26 S. Wiederhorn, *J. Am. Ceram. Soc.*, 1967, **50**, 407–414.
- 27 T. A. Michalske and B. C. Bunker, *J. Am. Ceram. Soc.*, 1987, **70**, 780–784.
- 28 R. Dauskardt, M. Lane, Q. Ma and N. Krishna, *Eng. Fract. Mech.*, 1998, **61**, 141–162.
- 29 T. Yoon, W. C. Shin, T. Y. Kim, J. H. Mun, T.-S. Kim and B. J. Cho, *Nano Lett.*, 2012, **12**, 1448–1452.
- 30 A. Ferrari, J. Meyer, V. Scardaci, C. Casiraghi, M. Lazzeri, F. Mauri, S. Piscanec, D. Jiang, K. Novoselov and S. Roth, *Phys. Rev. Lett.*, 2006, **97**, 187401.
- 31 R. Nair, H. Wu, P. Jayaram, I. Grigorieva and A. Geim, *Science*, 2012, **335**, 442–444.
- 32 S. P. Koenig, N. G. Boddeti, M. L. Dunn and J. S. Bunch, *Nat. Nanotechnol.*, 2011, **6**, 543–546.
- 33 J. H. Mun and B. J. Cho, *Nano Lett.*, 2013, **13**, 2496–2499.
- 34 X. Li, Y. Zhu, W. Cai, M. Borysiak, B. Han, D. Chen, R. D. Piner, L. Colombo and R. S. Ruoff, *Nano Lett.*, 2009, **9**, 4359–4363.